Impact of coating development on the hydraulic and transport properties in argillaceous limestone fracture

Catherine Noiriel, Benoît Madé, Philippe Gouze

Impact of coating development on the hydraulic and transport properties in argillaceous limestone fracture

Catherine Noiriel,[1,2,3] Benoît Madé,[1] and Philippe Gouze[2]

Received 1 August 2006; revised 27 April 2007; accepted 7 May 2007; published 12 September 2007.

[1] Results are reported for an acidic water flow-through experiment conducted in a fractured argillaceous limestone sample (73% carbonates). The change in fracture geometry and related parameters is reported for six data sets obtained from synchrotron X-ray microtomography experiments. High-resolution three-dimensional images of the sample allowed quantification of the changes in fracture morphology at a spatial resolution of 6 μm. Mineral mass loss and permeability changes in the sample were also determined. Several physico-chemical phenomena were identified during the experiment. Initial smooth fracture surfaces evolved rapidly toward rough surfaces with uneven clay coverage due to the preferential dissolution of carbonate minerals compared to clay minerals whose dissolution rate is about 10^6 slower. A microporous clay coating progressively developed at the fluid-rock interface during heterogeneous dissolution of the fracture, while the global dissolution rate of the fracture walls exponentially decreased. The increase in surface roughness and the presumed reorganization of clays caused a progressive reduction in permeability. During the last flow-through stage, a large decrease in sample permeability was attributed to the large removal of clay particles; this process was responsible for a dramatic collapse of the fracture walls near the sample inlet and led to the development of preferential flow pathways. The development of the clay coating also acted as a barrier to flow and mass transfer between calcite grains and bulk solution and affected transport processes within the fracture.

Citation: Noiriel, C., B. Madé, and P. Gouze (2007), Impact of coating development on the hydraulic and transport properties in argillaceous limestone fracture, *Water Resour. Res.*, *43*, W09406, doi:10.1029/2006WR005379.

1. Introduction

[2] An understanding of fluid-rock interactions in carbonate rocks and their impact on hydraulic and transport properties is important in Earth sciences to explain the effects of weathering, the natural development of karst, or to predict the anthropogenic consequences of acidization or carbon dioxide sequestration in carbonate reservoirs. In addition, fractures often constitute preferential paths for flow in low-permeable media. Their presence can lead to rapid transfer for fluids or pollutant over large distances. So far, experimental and numerical investigations regarding fracture properties have mostly focused on the description of the surface roughness and fracture aperture, which both control the head losses and determine the possible localization of flow [*Brown*, 1987; *Brush and Thomson*, 2003; *Dijk et al.*, 1999; *Glover et al.*, 1997; *Hakami and Larsson*, 1996; *Méheust and Schmittbuhl*, 2000; *Thompson and Brown*, 1991; *Zimmerman et al.*, 1992; *Zimmerman and Yeo*, 2000].

[3] However, fluids are not necessarily thermodynamically equilibrated with rock minerals within which they flow. So rocks located near the Earth's surface are subject to alteration by the circulating fluids and geometry can be considered as a parameter evolving with time. The evolution of porosity in freshly fractured rocks is highly controlled by the initial distribution of the fracture aperture, the fluid chemical composition and the flow regime. Modification of the fracture geometry by dissolution or precipitation processes can considerably alter the flow and transport properties in fractured media. It is expected that the permeability increases when the porosity increases, and so models have been proposed to relate these parameters, mainly for porous media [*Carman*, 1937; *Scheidegger*, 1957]. In fractured media, aperture growth by dissolution can increase the local transmissivity, typically resulting in larger local flux and mineral dissolution rate [*Ortoleva et al.*, 1987a, 1987b; *Steefel and Lasaga*, 1990]. Positive feedback can occur, leading to instability and dissolution fingering, as observed in experimental [*Detwiler et al.*, 2003; *Durham et al.*, 2001; *Polak et al.*, 2004] and numerical studies [*Békri et al.*, 1997; *Cheung and Rajaram*, 2002; *Hanna and Rajaram*, 1998].

[4] However, predictive models are often idealized because of the complexity of interactions in natural environment, and they rarely take into account all the phenomena that can take place within a fracture. Consequently, there are particular cases where predictions of these numerical codes fail and fractures may dissolve or collapse far more rapidly, and even contrary to what is predicted by the models. For

[1]Centre de Géosciences, École des Mines de Paris, Fontainebleau, France.
[2]Laboratoire Géosciences, Université de Montpellier II, CNRS, Montpellier, France.
[3]Now at Laboratoire Processus et Bilans des Domaines Sédimentaires, Université de Lille I, CNRS, Villeneuve d'Ascq, France.

0043-1397/07/2006WR005379

example, experimental observations in a fracture indicated that the permeability can decrease despite net dissolution, principally due to mechanical effects involving the closure of the fracture [*Durham et al.*, 2001; *Polak et al.*, 2004]. So the acquisition of experimental data from laboratory or field scale is required to validate the results given by models and to extrapolate theses results in the long term. Nevertheless, the majority of experimental works refers to relatively simple rock mineral assemblage (e.g., pure limestone) even though natural rocks present a large spectrum of mineralogical assemblages. About that, [*Weisbrod et al.*, 2000] pointed out the problem of using artificial and uncoated fracture in the laboratory to represent natural fracture flow conditions. The influence of rock-associated minerals is therefore often underestimated. The mineralogy of the rock matrix may have a significant influence on the dissolution rates and transport process, as pointed out by *Dijk et al.* [2002] and *Noiriel et al.* [2007]. Their studies suggest that coupled flow and dissolution processes are much more complex and unpredictable than commonly assumed.

[5] In carbonate environments, calcite is often associated with other primary or secondary minerals, such as clays, dolomite or quartz. The proportion of each mineral in original sediment depends on the geological origin of the different chemical elements and on the energy of the depositional environment. After deposit of the sediment, transformations and spatial reorganization of the different minerals result from diagenetic events that lead to numerous textural arrangements. Among the diversity of carbonate rocks that can be found in nature, argillaceous limestone is widely distributed throughout the Earth's crust. It is expected that the dissolution rate depends on the mineralogical and textural composition of the rock matrix, the reactive surface area of the minerals, the occurrence of a surface coating and the saturation index of minerals according to the chemical composition of the aqueous solution. The flow rate can also have an influence on the dissolution kinetics if the global reactions are controlled by the transport of chemical elements [*Murphy et al.*, 1989; *Rickard and Sjöberg*, 1983]. In this case, the thickness of the diffusion layer adjacent to the interface plays a role in the dissolution kinetics. A number of recent studies have focused on the impact of weathering on the dissolution rate and the modification of element transport [*Crovisier et al.*, 2003; *Cubillas et al.*, 2005; *Weisbrod et al.*, 2000; *White et al.*, 1999]. Most of the time, a systematic decrease in natural rate of weathering is observed with time. For example, *White and Brantley* [2003] and *Techer et al.* [2001] observed a significant parabolic decrease of silica concentration during weathering of silicate rocks or nuclear glasses. According to *White and Brantley* [1995], different phenomena can be involved in this decrease, such as precipitation of secondary minerals, adsorption of organic compounds, and etch pit developments at the surface. Moreover, some authors [*Ledieu*, 2004; *Techer et al.*, 2001], who observed the formation of a residual gel composed of insoluble products from the chemical reaction on the nuclear glass surface, suspected the gel to slow down the migration of dissolved ions in the solution.

[6] Conversely, chemical weathering is shown potentially to increase surface pitting and consequently reactive surface area. For example, *Anbeek* [1992] reported surface roughness more than 3 orders of magnitude higher for altered silicate minerals compared to fresh minerals. However, *White and Brantley* [2003] observed that the plagioclase dissolution kinetics decreases both in an altered and fresh granite despite the increase of surface area measured by the Brunauer, Emmet and Teller (BET) method [*Brunauer et al.*, 1938]. In addition, the surface area of the weathered granite was initially 1 order of magnitude greater than that of the fresh granite. These observations suggest that the surface which increases is not related to an increase in the surface area of reactive minerals, but rather to an increase in the surface area of insoluble residues. *Gautier et al.* [2001] suggested that the observed increase in surface should be related to an increase in pit surface which is little or nonreactive. The difficulty in assessing physical surface areas and in discriminating reactive from nonreactive surface produces a greater variability in measurement methods and in experiment interpretation.

[7] Variations in surface area can also be related to the development of an altered coating at the mineral or fracture surface, due to the differential rate of dissolution between the different minerals forming the rock matrix. For example, *White et al.* [1999] observed in their column experiment that the calcite was preferentially removed under natural weathering conditions. A microporous coating layer on a fracture surface can alter the surface area and its roughness [*Weisbrod et al.*, 2000]. When studying alteration in fractured chalk, these authors were able to measure the surface topography using a laser-scanning device. However, when a coating layer begins to form, complex three-dimensional (3-D) features develop at the fracture walls [*Gouze et al.*, 2003] and methods to measure surface topography in two dimensions, such as profilometry method [*Schmittbuhl et al.*, 1995], are no longer suitable. Moreover, this method fails to measure the coating growth, which is relevant of a 3-D process. Thus it is necessary to follow these processes using noninvasive and nondestructive methods.

[8] In this paper, we present laboratory observations on the impact of microporous coating development on fracture geometry, flow and reactive transport. This study examines the dissolution effects caused by acidic water within a natural fracture in an argillaceous limestone sample, specifically examining the evolution in the geometry and hydraulic properties in relation to the fluid chemistry. Our experimental methodology combines chemical analysis of the fluid, continuous measurement of fracture permeability and periodic characterization of the fracture geometry using noninvasive X-ray microtomography imaging. The measurements of permeability, porosity, mechanical aperture and the observation of geometry changes provide constraints for the understanding of processes controlling dissolution in the fracture. The method allows quantification of the effects of the microporous clay coating development on the global dissolution rate of the sample and the changes in mechanisms controlling the transport processes.

2. Experimental Methods

2.1. Flow-Through Experiment

[9] The flow-through experiment was conducted on a cylindrical core of argillaceous limestone. The rock, a micritic carbonate rock of Valanginian age (lower Creta-

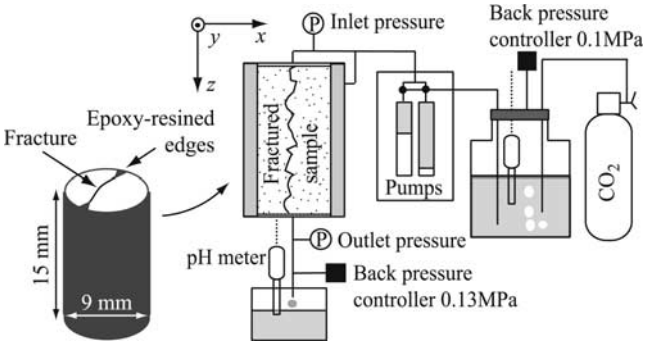

Figure 1. Schematic description of the experimental setup.

ceous), was sampled in a borehole drilled in the Montpellier area (southeast of France). Fresh fractures were present in the cutting, as a result of damage caused during the drilling procedure. A core of 9 mm in diameter and 15 mm in length was prepared to suit the optimal size for the X-ray microtomography procedure. The sample was cored to produce a longitudinal fracture subparallel to the rotation axis of the cylinder. Note that the fracture plane was oriented approximately 80 degrees to the bedding plane. The two faces of the core were assembled using epoxy resin to prevent any mechanical displacement of the fracture walls during the experiment. The core was silicone coated and jacked with a Teflon® membrane to seal its periphery. Then the core was placed in the flow-through cell.

[10] The experiment was conducted at room temperature (about 20°C). The core sample was initially saturated with water under vacuum. The sample was installed in the percolation cell and submitted to an acidic fluid flow. The confining pressure was maintained at the same fluid pressure at the sample inlet. The inlet fluid used in the experiment was 0.010 ± 0.001 mol L^{-1} NaCl solution prepared from reagent-grade NaCl diluted in deionised water; the fluid, initially degassed, was maintained equilibrated during the experiment with carbon dioxide at a partial pressure of 0.10 ± 0.01 MPa using a calibrated back-pressure controller. The pH at the inlet was recorded continuously in the fluid to detect potential CO_2 saturation changes ($pH = 3.9 \pm 0.1$).

[11] The fluid was injected into the sample at a constant flow rate. The flow rate was controlled by a dual-piston pump. The applied flow rate was 300 cm^3 h^{-1} (8.33×10^{-8} m^3 s^{-1}) during the first stage of the experiment and 100 cm^3 h^{-1} (2.78×10^{-8} m^3 s^{-1}) during the four following stages. Pressure was measured at the sample inlet in the range 0 ± 0.0015 to 3 ± 0.015 MPa using a computer-controlled two-stage pressure sensor system in order to increase the accuracy in the ranges 0–0.3 MPa and 0–3 MPa according to the value of the inlet pressure. The pressure at the outlet was maintained constant at about 0.13 MPa using a calibrated back-pressure controller to avoid CO_2 degassing in the circuit. The pH and pressure at the inlet and outlet were recorded continuously using a Keithley KPCI-3116 acquisition card monitored with a Labview® program. A schematic representation of the percolation apparatus is given in Figure 1.

[12] Five flow-through stages of duration $\Delta t = t_{i+1} - t_i$ were conducted. A total of six scans were taken for the sample: at the initial state ($t = t_0$) and after each stage of dissolution ($t = t_1$ to t_5), i.e., after 4.5, 14.5, 29.5, 54.5, and 99.5 hours from the start of the experiment, respectively. Inlet fluid was analyzed prior to CO_2 saturation and effluents were sampled recurrently. Samples were collected for chemical analysis of the major cation concentrations using inductively coupled plasma–atomic emission spectrophotometer (ICP-AES).

2.2. A 3-D Microstructure Study With X-Ray Microtomography

[13] The structural morphology of the sample was characterized throughout the experiment using X-ray computed microtomography (XCMT). This device is a noninvasive, nondestructive 3-D radiographic imaging technique based on the X-ray attenuation (absorption) by materials (for example [*Mees et al.*, 2003]). The method is based on the 3-D reconstruction of an object from its 2-D projection data. Projections are obtained by measuring the X-ray attenuation coefficient of the sample at different angles. Because the amount of attenuation depends on the elemental composition of the object (the attenuation coefficient of a material μ_{att} increases with the increasing of the atomic mass), mineralogical constituents as well as pores and fractures can be differentiated on the 3-D X-ray absorption image. The facility used in this research resided on beam line ID19 at the European Synchrotron Radiation Facility (Grenoble, France). Synchrotron radiation has several advantages over traditional X-ray sources including homogeneous, parallel, monochromatic, and highly coherent photon flux.

[14] The sample was scanned with an X-ray beam energy of 40 keV. One thousand projections (radiographs) of the sample were taken every 0.18° for an angle θ ranging from 0 to 180 degrees, as the specimen sat on a rotation stage; so that the radiographs were taken parallel to the core axis. The monochromatic incident beam passed through the sample and the transmitted beam struck a scintillator that converts the transmitted X-ray photons into visible photons. The image on the scintillator was transferred to a 12-bit coupled charge device (CCD) FReloN (Fast Readout Noise) camera that converts images into digital data. The radiographic image for each projection of 2048×2048 pixels was stored in 16-bit raw file. The pixel resolution of the system was dictated by the combination of the selected optics with the CCD camera. The optical system used in the experiment provides a spatial resolution of 4.91 μm (pixel size) for an optical resolution of 6 μm. As the sample was longer than the height of the beam, only the upper part of the sample close to the inlet was scanned.

[15] Before reconstruction, radiographs were corrected for the variation of the X-ray beam intensity and for the background noise, by subtracting for each data frame white field, i.e., radiographs without the sample, and dark field, i.e., radiographs without the beam. Radiographs were also filtered with a conditional median filter in order to eliminate random noise due to high-energy scattered photons that may go through the lead shield of the camera. A back-projection algorithm was used to reconstruct the 3-D volume structure from the 2-D radiographs [*Herman*, 1980]. In the present study, the HST software (for High Speed Tomography) based on Fourier inversion was used (A. P. Hammersley, http://www.esrf.fr/computing/scientific/HST/HST_REF/hst.html, 2001). The reconstruction provides a 32-bit data

set which represents a 3-D image of the X-ray absorption for the different materials in the sample. For data manipulation, the 32-bit data sets were converted into 8-bit grey scale images (each voxel takes a value between 0 and 255) to reduce the size of the files by a factor of 4. Brightness is proportional to X-ray absorption. Hence dark voxels correspond to low-density phase, whereas white voxels correspond to high-density phase. Assuming that the composition and the density of the matrix and the porous phase are unchanged, differences in the image brightness and contrast are attributed to variation in the X-ray beam properties or to uncontrolled alteration in the condition of data acquisition. To achieve consistency in dynamic range of intensity values for the different data sets, the histograms of grey level distribution were normalized using a linear interpolation procedure. After that, the matrix and pore phases have the same grey scale on the different images.

[16] Results presented in this paper correspond to six volumes, V_{t0} to V_{t5}. The whole 3-D images of about 8600 millions voxels (2048 × 2048 × 2048) are reduced to fit the area where the fracture is situated. Each of the data sets contains about 980 millions voxels (350 × 1750 × 1600) corresponding to the same part of the fractured area imaged at time t_0 to t_5, respectively. A voxel is defined as a pixel cubed and is represented through a volume of 4.91 × 4.91 × 4.91 μm^3.

2.3. Data Analysis

[17] Concomitant analysis of the fracture geometry and aperture evolution was performed using three different methods: the XCMT imagery of the mechanical aperture, the monitoring of the equivalent hydraulic aperture, and the deduction of the chemical aperture using a mass balance approach. In addition, observations of the fracture surface morphology and surroundings were done using scanning electron microscopy (SEM), which provides high-resolution observations.

2.3.1. Mineralogical, Textural, and Chemical Analysis of the Sample

[18] The mineralogical composition of the sample was determined using X-ray diffraction (XRD) and completed by X-ray fluorescence spectrometry on rock powder. The textural description by image analysis of argillaceous limestone is difficult to obtain with optical microscopy on a thin section because of the fine-grained matrix, the high birefringence of the calcite and dolomite, and the presence of the clay-like phase. For these reasons, observations were made using SEM. Because SEM observation requires a fine carbon coating to be applied on the surface to be examined, observation of the initial surface morphology was made on the fracture surface of a similar sample fractured under the same conditions. Observation of the fracture morphology after experiment was made using scanning electron microscopy by detection of backscattering secondary electrons (BSE). Secondary electron mode (SE) was also used to directly study the surface topography of the fracture walls.

[19] The rock, a slightly dolomitic argillaceous limestone, consists of submicrometer calcite and dolomite crystals rimmed with clays. Dolomite crystals often present a particular morphology; despite their euhedral morphology, the intensity of backscattering becomes more pronounced toward the crystal periphery, indicating a change in the chemical composition of the crystal. Thus analysis of the different elements using X-ray energy dispersive spectroscopy (EDS) indicated that the crystal periphery contains more calcium and less magnesium than the crystal core, suggesting a dedolomitization process during the diagenetic reactions, with preservation of the original zoning with the dolomite. Some micrometer-sized quartz crystals and framboid pyrite were also observed. The results of X-ray diffraction on the full solid phase showed a strong calcite peak, with much smaller peaks of dolomite, clays and quartz. No magnesian calcite was detected in the sample. The results of X-ray diffraction on the separated clay fraction showed that it is composed, in decreasing order of significance, of kaolinite, illite, interstratified illite-smectite (~5%), probable chlorite-illite and chlorite.

[20] In order to determine the distribution of calcium and magnesium among the different minerals, two powder-crushed samples were prepared and weighed. The first was immersed in a mixed HCl-30% HF-30% solution at 60°C for 24 hours, to allow full dissolution of the solid phase. The second was immersed in HCl-30% at 60°C for the same time period to dissolve the carbonate phase. The total aqueous concentrations were determined using an ICP-AES. The chemical results are very similar, indicating that these ions are present primarily in the carbonate phases.

[21] In order to check more precisely the ratio between the different minerals in the rock sample, major elements were analyzed in a fused glass bead using X-ray fluorescence spectrometry (XRF). Since only five major mineral compositions are present in the carbonate rock (calcite, dolomite, clays, quartz and pyrite), it is possible to deduce the proportion of each mineral in the rock. Si content was assigned both to clays and quartz. It is not possible to discriminate between quartz and clay minerals based on Si content, but XRD data show quartz to be a very minor component compared to clay minerals. Mg and Fe content were entirely assigned to dolomite and pyrite, respectively. Ca content was assigned to dolomite and calcite. This analysis showed the sample to be composed of 65% calcite, 26% silicate minerals (essentially clays), 8% dolomite, and 1% pyrite. Calcite comprises 89% of the carbonates; dolomite comprises 11%.

2.3.2. Fracture Volume and Aperture Changes From Chemical Measurement

[22] Thirty-five water samples were collected from the outlet side throughout the experiment for chemical analysis of Ca, Mg, Na, Si, and K using ICP-AES. The sample volume changes were evaluated from the Ca and Mg amount removed by the acidic fluid percolating through the sample. The mass of Mg, n_{Mg} (mol) was assigned to dissolution of dolomite $CaMg(CO_3)_2$, Ca mass minus Mg mass, $n_{Ca} - n_{Mg}$, was assigned to calcite $CaCO_3$. Dissolved calcium and magnesium carbonates were calculated, based on the molar volume of these minerals. Assuming that the clays do not dissolve during the experiment (see section 4.2), the change in the fracture volume was then evaluated and compared to the 3-D images of the sample. The volumes of dissolved dolomite and calcite were calculated according to

$$\frac{\delta V_{rock}}{\delta t} = \frac{\delta V_{cal}}{\delta t} + \frac{\delta V_{dol}}{\delta t} = -Q\left(\upsilon_{cal}\left(C_{Ca} - C_{Mg}\right) + \upsilon_{dol} C_{Mg}\right) \quad (1)$$

where V_{rock}, V_{cal}, and V_{dol} are the volume of rock dissolved, the volume of dissolved calcite, and dolomite, respectively [L^3]; υ_{cal} and υ_{dol} are the molar volume of the dolomite and calcite minerals, respectively [L^3 mol^{-1}] (υ_{cal} = 36.93 cm^3 mol^{-1} and υ_{dol} = 34.90 cm^3 mol^{-1}); C_{Mg} and C_{Ca} are the molar concentration of the Mg and Ca species at the outlet of the sample (concentrations are zero at the inlet), respectively [mol L^{-3}]; and Q is the volumetric flow rate [L^3 T^{-1}].

[23] The rate of aperture increase, da_c/dt, can be theoretically determined from measured effluent concentration removed by the sample during the dissolution experiment. This calculation enables the theoretical change in aperture to be determined from effluent concentrations and measured flow rates. The rate of aperture change [m s^{-1}] is given by

$$\frac{\delta a_c}{\delta t} = -\frac{1}{A_s}\frac{\delta V}{\delta t} = -\frac{Q}{A_s}\left[\upsilon_{dol} C_{Mg} + \upsilon_{cal}\left(C_{Ca} - C_{Mg}\right)\right] \qquad (2)$$

where A_s is the equivalent surface area of the fracture wall: $A_s = L \times l$ [L^2], where L [L] and l [L] are the length and the width of the fracture, respectively. The chemical aperture at time t_i, a_c, is obtained by integration of equation (2)

$$a_c = a_0 + \frac{Q}{A_s}\left(\upsilon_{dol}\int_{t_0}^{t_i} C_{Mg}\,dt + \upsilon_{cal}\int_{t_0}^{t_i}\left(C_{Ca} - C_{Mg}\right)dt\right) \qquad (3)$$

where a_0 is the initial sample aperture.

2.3.3. Determination of the Hydraulic Aperture

[24] The change in hydraulic aperture of the fracture was measured throughout the flow-through experiment by recording the differential pressure ΔP [M L^{-1} T^{-2}] between the sample inlet and outlet. The very low permeability of the rock matrix enables ΔP to be converted directly into the equivalent hydraulic aperture a_h [L], using the cubic law for the parallel plate approximation [*Zimmerman and Bodvarsson*, 1996]

$$a_h = \sqrt[3]{\frac{12\,\mu\,L\,Q}{\Delta P\,l}} \qquad (4)$$

where Q is the volumetric flow rate [L^3 T^{-1}], μ is the dynamic viscosity of the fluid [M L^{-1} T^{-1}], L is the length of the sample in the flow direction [L], ΔP is the differential pressure [M L^{-1} T^{-2}], and l is the width of the fracture [L]. Combining the cubic law with Darcy's law, permeability k [L^2] and hydraulic aperture are related through the expression $k = a_h^2/12$.

2.3.4. Analysis of Fracture Morphology and Mechanical Aperture Changes From 3-D Imaging

[25] To quantify parameters characterizing the fracture morphology changes from XCMT (e.g., porosity, fluid-rock specific surface area, fracture wall topography, surface roughness), images must be segmented; that is, the pixels belonging to the pore space must be distinguished from those belonging to the solid matrix. For that, it is necessary to identify the different phases, i.e., the solid and the fluid phase, in the images based on their intensity values. Thus the different phases were identified in the images due to their different X-ray absorption properties and hence the different intensity values on the grey scale histograms. In this case, the choice of the parameters for the segmentation is a very difficult task because the two phases (void and matrix phases) are not clearly separated on the grey scale histograms. As the data are noisy, a simplified threshold method would lead to significant errors. A segmentation technique based on region growing was preferred [*Pitas*, 2000]. Two seeds that contain only void or matrix voxels were initially chosen. Regions were grown from each seed by adding in neighboring voxels that are similar, increasing the size of the regions. The size of the regions increases until all the voxels are associated to the void or the matrix. The advantage of this local thresholding is to localize the edges separating the two phases, where the gradients are stronger. This is an important aspect of segmentation, particularly for images such as those produced by XCMT.

[26] Moreover a mixed phase, mainly composed of clays and dissolved carbonate mineral ghosts, developed during the experiment (see section 3.3). As this phase contains both voids and matrix, it cannot be clearly separated from the matrix or the void phase. So a three-phase segmentation procedure would fail. Nevertheless, it is possible to assign this phase either to the void phase or to the matrix phase. According to utility, two types of voxels can be identified: matrix plus mixed phase versus void phase or void plus mixed phase versus matrix phase. The choice of the appropriate parameters for segmentation was made according to a visual inspection of the segmented volumes B_{ti} by comparison to the grey scale volumes V_{ti}. The segmented volumes obtained, B_{ti}, are stored in a matrix of bytes, corresponding to binary values, either 0 for the matrix phase or 1 for the void phase. Then, the volumes were percolated with a fire grass algorithm [*Gonzales and Woods*, 1992] in order to identify the connected porosity from the total porosity. Subsequently, the fracture wall topography and aperture cartography were deduced from the segmented volumes B_{ti}.

[27] After the segmentation, the value of the local aperture, a, is defined as the distance between the two fracture walls in the $\vec{x}$ direction normal to the plane ($\vec{y}$, $\vec{z}$) (see Figure 1). The mechanical aperture a_m is defined as the mean of the local apertures

$$a_m = \langle a \rangle_{yz} = \frac{1}{Ll}\sum_{y=1}^{y=l}\sum_{z=1}^{z=L}\left(a_{y,z}\right) \qquad (5)$$

where L and l are the sample length and width [L], respectively. The standard deviation of aperture σ_{am} is defined as the root mean square deviation of the local aperture from the mechanical aperture

$$\sigma_{am} = \sqrt{\frac{1}{Ll}\sum_{y=1}^{y=l}\sum_{z=1}^{z=L}\left(a_{y,z} - a_m\right)^2} \qquad (6)$$

[28] Moreover it is possible to calculate the geometric surface area of the fracture walls (S_{walls}), by measuring the surface area of the void-matrix interface. As it is not relevant to express the geometric surface per unit of volume for a fracture (L^2 L^{-3}), we defined the specific surface

coefficient, which denotes the ratio of the measured surface area to an equivalent planar surface area

$$S_s = S_{\text{walls}}/Ll \tag{7}$$

[29] The surface roughness coefficient, $\Re$, which can be a good indicator of roughness changes at microscopic scale [*Myers*, 1962], is calculated from the variation of the two fracture wall elevations at t_0 and t_1, Δh, with

$$\Re = \sqrt{\frac{1}{Ll}\sum_{y=1}^{y=l}\sum_{z=1}^{z=L}\left(h_{y,z+1} - h_{y,z}\right)^2} \tag{8}$$

2.4. Error Analysis

[30] The major factors contributing to uncertainties in chemical aperture are the errors inherent in the analytical methods used and random errors in the measurement of the fluid effluent volume. A sample spike, a blank and calibration standards were used and replicate analyses were performed to assure accuracy and precision of the analysis and to monitor the ICP-AES instrument performance.

[31] The major factors contributing to uncertainties in hydraulic aperture are the errors inherent in the calibration of the pressure sensors and of the flow rate. Pressure sensors have high accuracy and stability. The maximal error is ±0.5% of the adjusted range (either 0.3 or 3 MPa). Moreover, the sensors were calibrated before each stage of the flow-through experiment. The flow rate provided by the pump was also calibrated, by measuring the volume of effluent delivered by each piston pump by unit of time. On the basis of these sources of uncertainty, the chemical aperture and hydraulic aperture values are good to a few percent.

[32] Estimating uncertainties in mechanical aperture from XCMT data is difficult because it depends on several parameters. Uncertainties associated with data acquisition are potentially time-dependent (e.g., X-ray beam stability, monochromator performance). However, both the ESRF X-ray source and the beam line ID19 are highly optimized, providing very reliable data. Conversely, uncertainties associated with the data processing are difficult to quantify. Specifically, the image segmentation is the least constrained step of the data processing procedure; it depends principally on the attenuation coefficient contrast between rock matrix and voids, and on the background noise. The precision of the measurement can be estimated from an examination of the grey level histograms for each volume V_{ti} (Figure 2). The histogram was clearly bimodal at the beginning of the experiment, and remained bimodal despite the progressive development of a mixed phase (i.e., the appearance of the clay coating, see section 3.3). To estimate the uncertainties introduced by the segmentation procedure, the distribution parameters of each phase (i.e., voids, matrix, and mixed) were calculated. Some voxels belonging to the void, the mixed, and the matrix phase were manually sampled for each volume. Grey value distributions can be approximated by Gaussian distributions, indicating that measurement noise is random. Using the mean and the variance of each Gaussian distribution, the different distribution intensities were then normalized to best fit the experimental histograms (Figure 2).

[33] For volumes V_{t0} and V_{t1}, void and matrix peaks are well separated on the histogram. Voxels that are not covered by the Gaussian reference curves correspond to indeterminate voxels located at the interface between the void and the matrix. As these voxels are partially composed by void and matrix, their grey value is linearly proportional to the percentage of void and matrix in this voxel; but their value is modulated, as is the grey value for each voxel, by the random noise. The region-growing algorithm allows separation of the whole image into two phases, by assigning indeterminate voxels to either the void or the matrix phase. The void and matrix distributions are well separated on the histogram, and therefore different choices of seeds will give almost identical results. In the absence of background noise, the error in determining the position of the interface is at most one half of the voxel size and on average one fourth of the voxel size. As the fracture void is bounded by two fluid-rock interfaces, the resulting error on the mechanical aperture calculation is ±2.45 μm. Because of inherent noise, the error is slightly greater, but difficult to estimate. Assuming that the uncertainty in the position of the boundary between void and matrix is limited to one voxel, the error in the mechanical aperture measurement is approximately one voxel width, i.e., ±5 μm.

[34] For volumes V_{t2} to V_{t5}, the situation is much more complex because the distributions of the different phases overlap (Figure 2), indicating that some void voxels can have the same grey level as mixed-phase voxels, or that mixed-phase voxels can have the same grey level as matrix voxels. Using appropriate parameters in the region-growing segmentation algorithm allows separating these different phases, but the results depend on the choice of the seeds. Thus the error in a_m for theses volumes is greater than that for V_{t0} and V_{t1}. By visually comparing the initial (V_{ti}) and the segmented volume (B_{ti}), the error can be estimated to be approximately three voxel widths, i.e., ±15 μm.

3. Results

[35] Coupling the flow-through experiment with the XCMT observations provides from the microscale (local scale) to the sample-scale (global scale) three independent evaluations of the parameters characterizing the dissolution process within the fracture. Differential pressure measurement between the sample inlet and outlet allows quantification of the hydraulic aperture. In addition, differential measurement of the chemical elemental concentration in the fluid inlet and outlet characterize the dissolution kinetics at the sample scale. Because of the nondestructive nature of the microtomography imaging, we could also observe progression of the chemical reaction over the fracture geometry and the related morphological changes.

[36] The two walls of the fracture did not dissolve uniformly during the experiment. Calcite and dolomite dissolved more rapidly than quartz and clays. Despite the removal of carbonate minerals, the fracture did not open and the development of a clay coating caused the fracture to clog. The presence of the microporous clay fraction caused the global dissolution rate of the sample to progressively decrease. Results of aperture measurement are then dis-

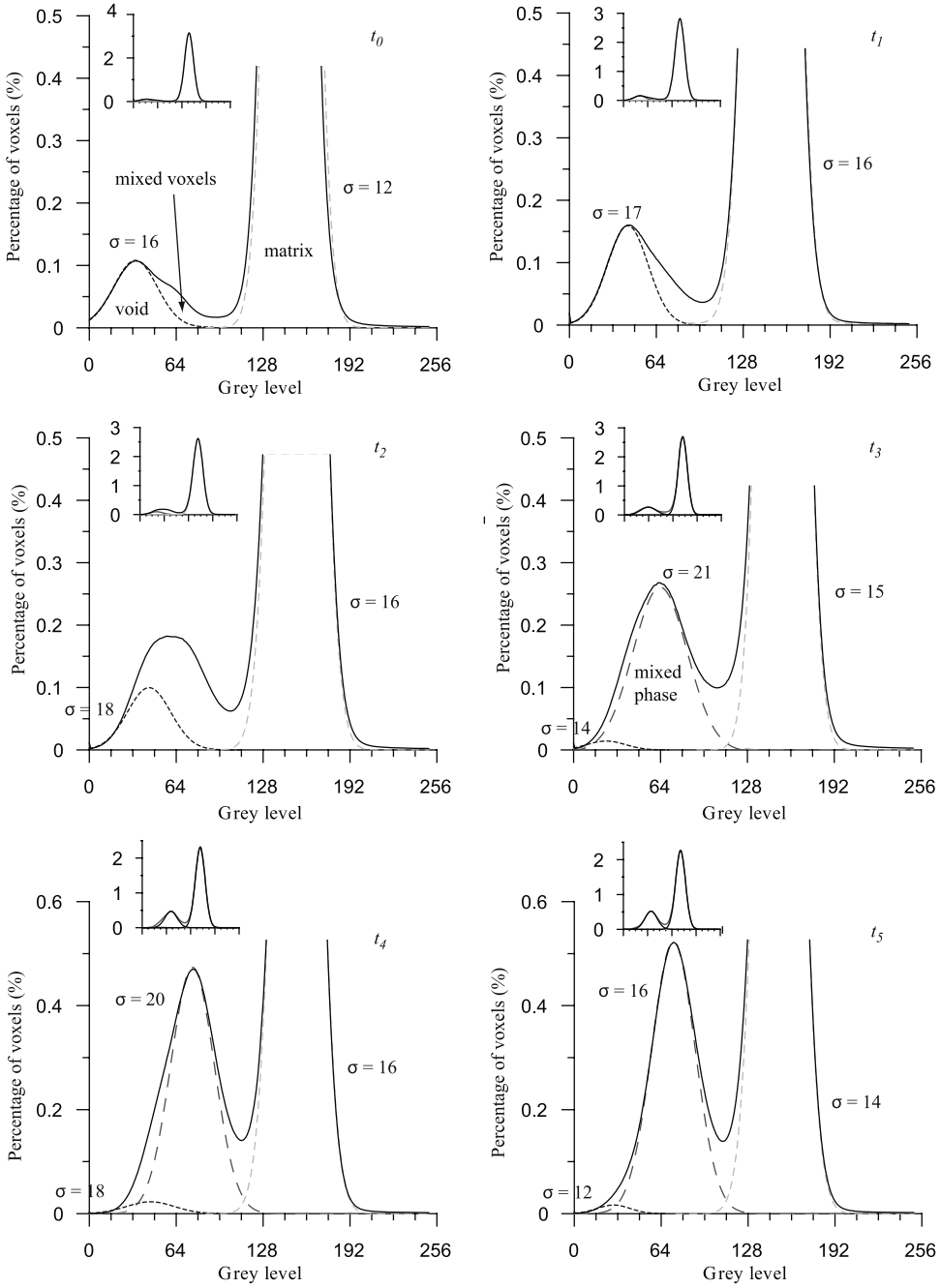

Figure 2. Histograms of the different volumes V_{t0} to V_{t5}. Black solid lines denotes the histograms obtained using XCMT, and dashed lines are the best fitted Gaussian distributions for the individual phases, i.e., void (black), mixed (dark grey), and matrix (light grey). Standard deviations (σ) of the Gaussian distributions are given.

cussed and a diffusion-limited model for transport within the fracture is proposed.

3.1. Porosity Changes From Mineral Mass Balance

[37] The volume of minerals removed during each flow-through stage was deduced from the cation concentration in the effluent solution (equation (1)). The results are presented in Table 1. The calcite and dolomite were progressively dissolved, and the porosity increased. At the end of the experiment, 31.8 mm^3 of calcite and 2.0 mm^3 of dolomite were dissolved, bringing the total amount removed to 33.8 mm^3. The increase of the equivalent chemical aperture a_c was 283 μm.

3.2. Equivalent Hydraulic Aperture

[38] The initial equivalent hydraulic aperture of the fracture, a_h, was about 50 μm. In the first stage of experiment, the permeability, k, decreased slightly, from 2.09×10^{-10} to 1.95×10^{-10} m^2, corresponding to a reduction of a_h from 50 to 48 μm. During the other stages of the experiment, the permeability and therefore a_h also reduced progressively, as presented in Figure 3. Results for equivalent hydraulic

Table 1. Summary of the Experimental Results

	Initial $t = t_0$	Stage 1 $t_0 < t \leq t_1$	Stage 2 $t_1 < t \leq t_2$	Stage 3 $t_2 < t \leq t_3$	Stage 4 $t_3 < t \leq t_4$	Stage 5 $t_4 < t \leq t_5$
Flow rate, $cm^3\ h^{-1}$		300	100	100	100	100
Duration Δt, hours		4.5	10	15	25	45
Dissolved volume, mm^3		3.3	7.9	13.3	18.5	33.8
Dissolved calcite, mm^3		3.2	7.5	12.5	17.5	31.8
Dissolved dolomite, mm^3		0.1	0.4	0.8	1.0	2.0
Permeability k, $\times 10^{-12}\ m^2$	209	209-195	155-110	130-95	80-60	90-8.5
Hydraulic aperture a_h, μm	50	50-48	44-37	39-34	31-27	32-10
Mechanical aperture a_m, μm	59	86	52	61	67	30
σ_{a_m}, μm	20	21	21	24	25	21
Chemical aperture a_c, μm	(59)	87	125	170	214	342

aperture from the different stages of the experiment are reported in Table 1. As shown in Figure 3, slight discontinuities can be observed in the permeability and the hydraulic aperture determination between the different stages of the experiment. That can be explained by minor modifications of the fracture wall geometry between two stages of the experiment. In fact, as the tomography acquisition was spread over several months, the sample was partially desaturated during two percolation stages and removal of particles was observed during the resaturation. Between t_4 and t_5, two sudden large pressure drops (from 0.075 to 0.15 MPa after 75 hours and from 0.285 to 0.5 MPa after 94 hours of experiment) involved instantaneous reduction in aperture (from 20.5 to 16 μm after 75 hours and from 13 to 11 μm after 94 hours). Globally, the a_h value was reduced from 50 to 10 μm during the experiment. Note that the increase of effective pressure in the sample does not cause the aperture to change because the two fracture walls are epoxy coated on their edges to avoid possible closure of the fracture with an increase in pressure.

3.3. Mineralogy Driven Dissolution From Imaging

[39] The change in fracture geometry and related parameters was monitored using X-ray microtomography. Additional SEM observations of the fracture morphology after the experiment confirms the observations made with XCMT. Figure 4 presents an XCMT cross section of the fracture at the start and after the different stages of the flow-through experiment. Note that the various images cannot be exactly superimposed, explaining slight differences in the spatial representation of the fracture morphology. It is possible to discriminate on Figure 4 the pyrite minerals (in white) from the other minerals forming the matrix. During t_1, the fracture appeared to have widened; but on a small scale, the boundary between fracture and matrix is not clear. Because of differential dissolution rates between the minerals, some irregularities developed at the fluid-rock interface. The fracture did not dissolve uniformly, and clay minerals remained at the fluid-rock interface. After t_1, the carbonate minerals around the fracture continued to dissolve and a clay coating displaying overhangs progressively developed and covered the two fracture walls entirely. The thickness of the clay layer progressively increased with time. At t_5, a large part of the fracture void was clogged by the clay coating. Then, two channels of fluid flow clearly appeared on the two fracture edges (in contact with the glue), where the aperture was initially the largest. We can also observe from t_4 the opening of secondary fractures perpendicular to the main fracture, which may have resulted from the constant increase of confining pressure.

[40] The values of a_m are summarized in Table 1. For volumes V_{t0} to V_{t5} the segmentation was made in order to separate the mineral-containing phases (i.e., matrix and microporous clay coating) from the void geometry. In that case, the clay-like microporous phase is not considered to hydraulically belong to the fracture aperture even if it is in contact with the flowing water. The mechanical aperture increased during stage 1, but it is probably overestimated because of the difficulties in differentiating the clay-like phase from the void. After that, a_m decreased during stage 2, slightly increased during stages 3 and 4 and strongly decreased during the last stage. Conversely, the standard deviation of the aperture remained nearly constant during the experiment, the values of σ_{am} being comprised between 20 (at t_0) and 24 μm (at t_4) (Table 1).

[41] An additional segmentation procedure was performed for V_{t5} to separate the porous-containing phases (i.e., voids and microporous clay coating) from unaltered matrix; the volume obtained is called $B_{t5'}$. The image difference between volumes B_{t5} and $B_{t5'}$ makes it possible to compute the clay coating thickness and the volume variation between the beginning and the end of the experiment. Results show an average increase of 284 μm of the microporous clay coating. Considering that clays comprise

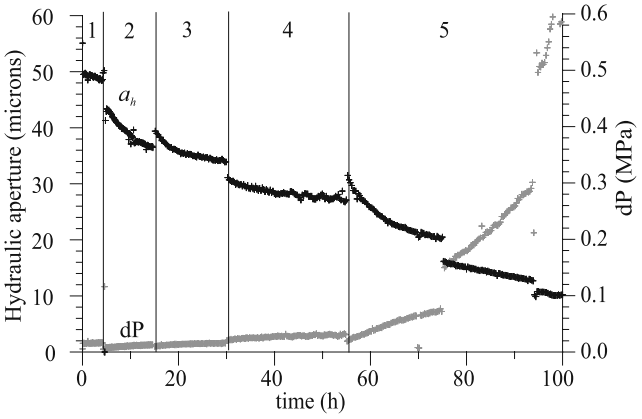

Figure 3. Change in equivalent hydraulic aperture over the duration of the experiment (black crosses) and related changes in differential pressure between sample inlet and outlet (grey crosses). The vertical lines determine the different stages of experiment.

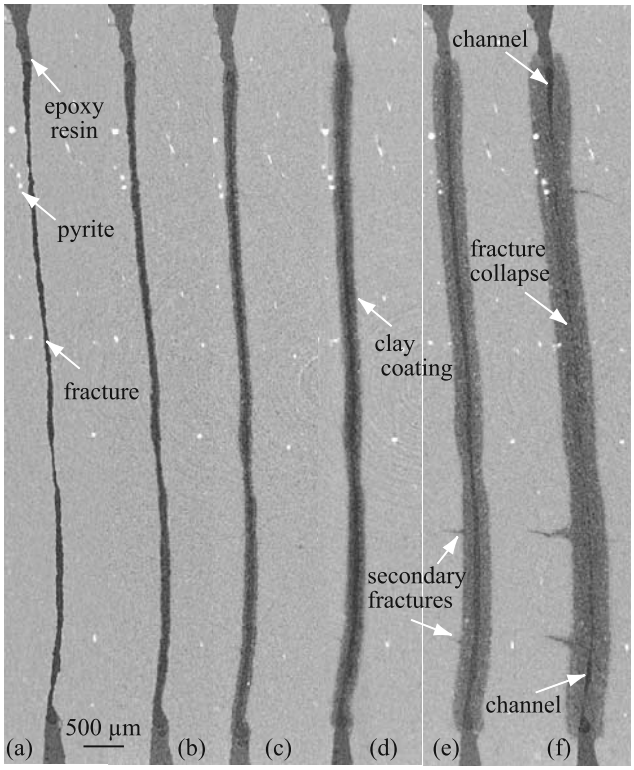

Figure 4. Cross sections of the fractured argillaceous limestone obtained by X-ray microtomography at times (a) t_0, (b) t_1, (c) t_2, (d) t_3, (e) t_4, and (f) t_5.

25% of the microporous phase, the coating represents a volume of clays close to 8.75 mm^3.

[42] SEM photomicrographs from a fractured reference sample, as well as from the postdissolution sample, were used to investigate precisely the dissolution effects on the fracture surfaces. Examination of the fracture wall morphology in secondary electron mode compared to the initial morphology (Figures 5a and 5b) shows the formation of many pits on the fracture wall surface. Clay coatings developed on both sides of the fracture voids (Figure 5c). It is also possible to detect the presence of pyrite, quartz and dolomite crystals in the clay coating, where calcite no longer appears. While the pyrite does not seem to be affected by the dissolution process, it is not the case for the dolomite. The quantity of dolomite appears to decrease with distance from the clay coating-matrix interface.

[43] Ghosts of dissolved euhedral dolomite crystals remained (Figure 5d), indicating that the clay structure is relatively well preserved during the experiment. Secondary microcracks which developed perpendicular to the main fracture can also be observed. The microcracks developed at the carbonate grain extremity, where the strain was probably lower. There is no relationship between the orientation of the microcracks and the bedding plane of the rock (visible with optical microscopy, but not under SEM observation). No shearing displacement of the microcracks was noticed, indicating that the secondary fracturing was not involved in the fracture clogging.

4. Process Basis for Fracture Geometry Changes

4.1. Impact of the Clay Coating on the Permeability Reduction and the Fracture Clogging

[44] Two distinct phenomena occurred within the fracture. Despite dissolution of the carbonate grains, a decrease

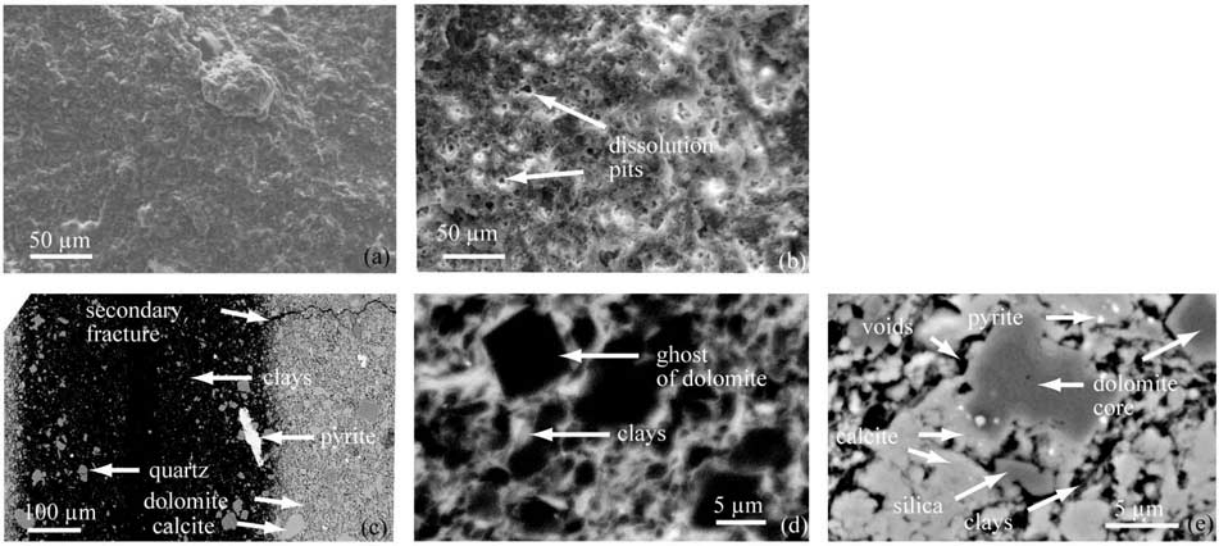

Figure 5. SEM images of the carbonate sample. (top) Secondary electron (SE) images of the fracture wall surface (a) before and (b) after the experiment. (bottom) Backscatter electron (BSE) images of polished thin section of the sample after the experiment: (c) cross section in the sample showing the microporous clay coating and the decrease of dolomite in the microporous phase from the fracture void toward the matrix; (d) enlargement of the microporous phase; (e) enlargement of the matrix phase. Light intensity in BSE image is proportional to the density, which allows distinction of porosity as well as between different minerals (clays, dolomite, calcite, or pyrite).

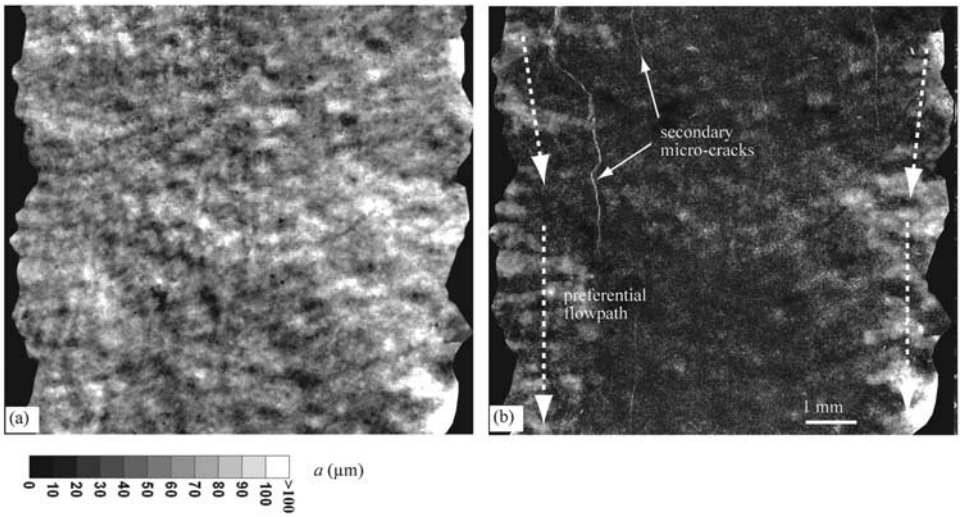

Figure 6. Cartography of aperture distribution (a) before (t_0) and (b) after the experiment (t_5). Blackish edges represent the epoxy glue.

in permeability is observed during the experiment, in two steps: (1) a progressive but slow increase of the differential pressure ΔP during the main part of the flow-through experiment and (2) a rapid increase with two sudden jumps of ΔP during the last flow-through stage. As mechanical displacement of the fracture walls was avoided by the epoxy glue placed on the fracture edges, only four mechanisms can be responsible for the fracture clogging: (1) clay swelling, (2) mechanical deformation of the sample, (3) local changes in the orientation of clay minerals, and (4) clay displacement and redeposition.

[45] The small reduction in a_h during each stage of the experiment can be explained by clay reorganization and possible swelling effects. As the rock contains some smectite minerals in the clay fraction, possible swelling (while the clay coating is growing) would affect the values of a_h, by reducing the fracture aperture at the boundary between water and clay coating. Swelling effects can occur during hydration in some phyllosilicate minerals that contain variable interlayer spacing. Smectite minerals can undergo as much as a 30% volume change due to wetting and drying cycles [*Komine*, 2004; *Norrish*, 1954; *Prost*, 1990]. The role of the smectite in the clogging mechanism of microcracks in altered volcanic rock was also underlined by *Serra et al.* [1998]. When fully hydrated, a smectite crystal can more than double in size from 0.9 nm to over 1.8 nm [*Bassett and Wu*, 1999; *Wersin et al.*, 2004]. However, the relative high ionic strength (0.01M NaCl) of the injected solution may reduce the thickness of the bonded water film in the interlayer, as a result of changes in osmotic pressure. Moreover, the interstratified illite-smectite clay mineral, which constitutes the potential swelling clay in the sample, is only about 5% of the total mineral fraction. Therefore clay-mineral swelling likely accounts for only a very small portion of the observed permeability decrease.

[46] However, the value of the coefficient $\Re$ increased from 0.84 to 1.61 during the first flow-through stage, indicating that the fracture wall roughness approximately doubled. This large increase in the surface roughness can increase the head losses near the fracture walls, explaining the slight permeability decrease during stage 1 of the experiment. Moreover the clays increasingly came in contact with the fluid as the carbonate grains dissolved. As the clays are not surrounded by the rigid calcite grain, they can freely deform themselves in the fracture void. Thus clay structure reorganization appears to be involved in the progressive permeability decrease throughout the experiment, although the presence of euhedral dolomite ghosts generally suggests minor structural rearrangement of clay minerals (see Figure 5e).

[47] The discontinuities in the a_h value between two stages of the experiment (Figure 3) can be attributed to particle displacement. A slight a_h jump can be attributed to the removal of particles, which was observed during resaturation of the sample in the percolation cell between stages; a slight a_h drop can be attributed to the removal of particles followed by a redeposition within the fracture. During stage 5, two significant and sudden jumps in ΔP measurement (Figure 3) are attributed to massive clay particle displacements in the fracture. It is possible to identify the collapsed areas in the clay coating by subtracting the image of aperture at the end of experiment (at t_5) from the image before experiment (at t_0) (Figure 6), or by computing the average aperture $\langle a \rangle_y$ along the flow axis (Figure 7). The aperture reduction is larger near the inlet of the sample than near the outlet (Figure 7), where an accumulation of clays has probably occurred. Consequently, the flow was focused along two preferential paths, which formed in the area where the aperture was initially larger (Figure 6).

[48] Secondary microcracks, which have been observed perpendicular to the main fracture on the XCMT images (see Figures 5 and 6) from stage 4 of the experiment, do not seem to be involved in the fracture aperture reduction. SEM observation at the grain boundaries does not show any displacement on either side of the microcracks. Moreover, no area of preferential aperture reduction is observed in proximity to the secondary microcracks when subtracting the image of aperture after experiment from the image before experiment (Figure 6).

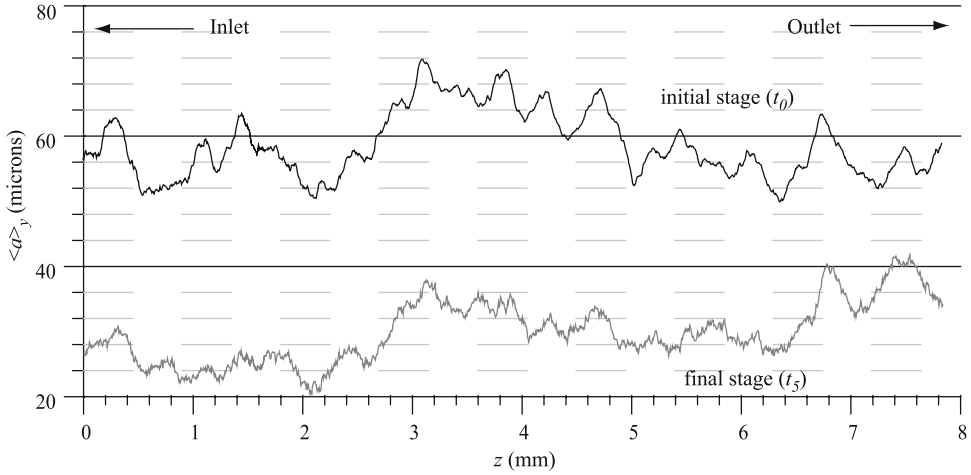

Figure 7. Aperture average on y direction along the flow (z direction).

4.2. Comparison for the Different Methods for Aperture Measurement

[49] Different approaches were used in this study to evaluate the fracture aperture. Figure 8 presents the different values of the three distinct apertures calculated with independent methods: (1) equivalent hydraulic aperture a_h, (2) chemical aperture measured from mineral mass balance a_c, and (3) mechanical aperture a_m. The results obtained by calculating aperture with different methods can be very different. At the beginning of the experiment, a_c, a_m, and a_h are similar in magnitude. However, after the first stage, the magnitude of a_c continues to increase whereas the magnitude of a_m remains variable but approximately constant and the magnitude of a_h progressively decreases. The different results reflect, in part, the heterogeneity of the matrix dissolution close to the fracture walls.

[50] The agreement is good between a_h and a_m at t_0, indicating that the assumption of the cubic law is valid for the unaltered fracture. The value of a_c is not directly measurable at the beginning of the experiment (only variation of a_c can be deduced during the experiment), so a_c was taken equal to a_m at t_0. At the end of the first stage, a_m and a_c are similar. During the first stage of the experiment, short-term dissolution effects are localized near the fracture wall surfaces. As the clay coating does not comprise a significant fraction of the space between the fracture walls and the unaltered matrix, the image-processing methods are most likely to yield accurate measurements of a_m. That is why the agreement is good between a_m and a_c. At the same time, a_h is lower than a_m because calcite dissolution pits are forming at the surface of the walls, and clay minerals have not yet become exposed. The consequence of this process is an increase in a_m, but since fluid is not flowing in such pits or dead ends, there is no reason for a_h to increase. Because the permeability depends on the fracture aperture properties, the increase in surface roughness between t_0 and t_1 (section 4.1) can reduce the permeability by introducing additional head losses near the fracture walls. This phenomenon can probably explain the slight decrease in a_h that is observed at this time.

[51] From t_1, it is obvious that interpreting changes in chemical aperture a_c as changes in the width of the flow path, and therefore permeability is inappropriate since the clay coating is being developed. Despite the dissolution of the carbonate minerals, a_h decreased and a_m is variable. Because of the development of clay coating, it is difficult to evaluate precisely the value of a_m because of the difficulties of distinguishing in the images the microporous clay coating from the void or matrix phase. Note that it would be meaningless to calculate the roughness exponent $\Re$ after the other stages of experiment since the fluid-rock interface is entirely covered by the clay coating. Moreover, the almost constant standard deviation of the aperture (σ_{a_m}) indicates that the changes in fracture do not affect the sample-scale aperture roughness (Table 1).

[52] Taken independently, these three approaches need to be interpreted differently to estimate the fracture geometry changes during the dissolution process. The value of a_c reflects the mass of calcite and dolomite dissolved, but is not relevant to interpret the fracture aperture evolution with time. The measurement of a_h is relevant to interpret the progressive closure of the fracture, but gives only an average size of the aperture, which does not reveal the heterogeneity of the aperture along the flow path. The use of

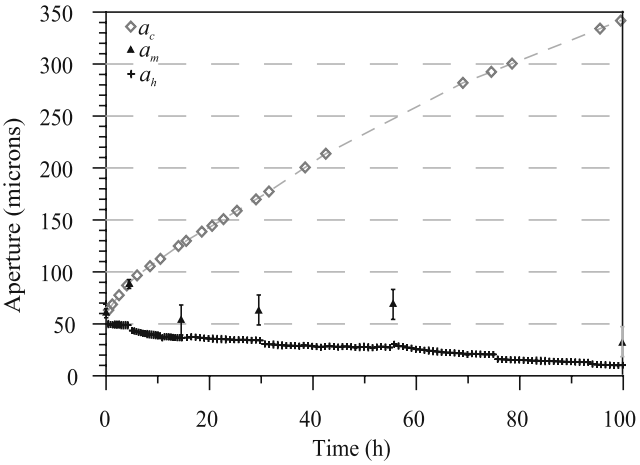

Figure 8. Comparison between changes in equivalent hydraulic aperture (crosses), mechanical aperture (triangles) and theoretical chemical aperture (diamonds) over the duration of the experiment.

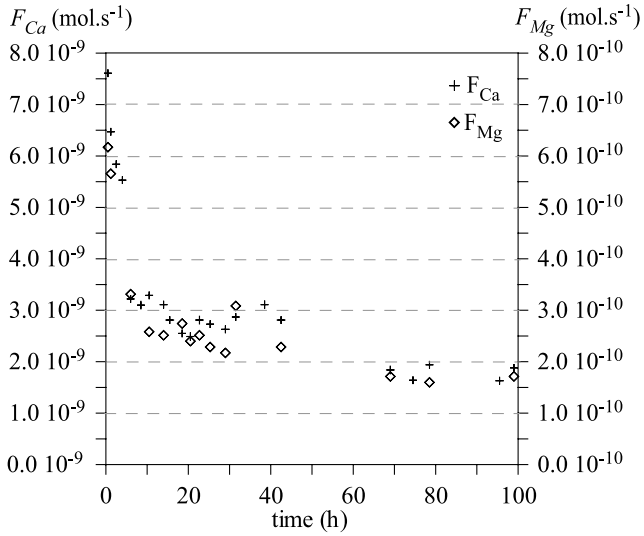

Figure 9. Chemical flux of Ca (F_{Ca}) (crosses) and Mg (F_{Mg}) (diamonds) at the outlet of the sample.

XCMT, within the limitation of resolution to distinguish clay minerals, enables a better understanding of the complex consequences of carbonate mineral dissolution within the fracture. Overall, the three approaches are complementary to interpreting the experimental results.

4.3. Chemical Rates of Dissolution

[53] The Ca and Mg concentrations can be related to the chemical reaction progress of calcite and dolomite dissolution, respectively. Experimental studies have shown that below pH 5.5, the calcite dissolution rate is pH-dependent and limited by mass transfer processes [e.g., *Plummer et al.*, 1978; *Sjöberg and Rickard*, 1984]. Therefore, within the fracture, the dissolution rate should increase with fluid velocity because the mass transfer of reactants and products is enhanced by the local fluid velocity near the mineral surface.

[54] In the experiment, the pH of the solution evolves from 3.9 at the sample inlet toward an average value of 4.6 at the sample outlet. The inlet solution of 0.01M NaCl water equilibrated with CO_2 at the partial pressure of 0.1 MPa is undersaturated with respect to the different minerals. The theoretical equilibrium pH of the inlet solution with the rock sample is calculated using CHESS [*van der Lee*, 1998], by equilibrating the different minerals identified in the XRD analysis with the solution. The resultant pH is 6.08, which is close to the pH in equilibrium with calcite (pH = 6.00), according to the reaction

$$CaCO_3 + H^+ \leftrightarrow Ca^{2+} + HCO_3^- \qquad (9)$$

[55] The residence time of fluid in the sample is short, so that the outlet fluid remains very undersaturated with respect to the different minerals ($\Omega_{calcite} \sim 10^{-5}$). Under acidic pH and far from equilibrium, the global dissolution rate r of calcite (mol s^{-1}) can be expressed as [*Plummer et al.*, 1978]

$$r_{cal} = S_{r(cal)}(k_1 a_{H^+} + k_2 a_{CO_2})(1 - \Omega_{cal}) \qquad (10)$$

[56] According to *Chou et al.* [1989], the global dissolution rate of dolomite is

$$r_{dol} = S_{r(dol)} \times \left(k_{1'} a_{H^+}^{0.75} + k_{2'} a_{CO_2}^{0.75}\right) \times (1 - \Omega_{dol}) \qquad (11)$$

where the k_i terms refer to a specific kinetic constant (mol m^{-2} s^{-1}), S_r designates the reactive surface area (m^2) and Ω signifies the mineral saturation index. Between pH 3.9 and 4.6, the dissolution rate decreases from 7.10 $\times$ 10^{-9} to 2.45 $\times$ 10^{-9} mol m^{-2} s^{-1} for calcite and from 1.02 $\times$ 10^{-9} to 8.46 $\times$ 10^{-10} mol m^{-2} s^{-1} for dolomite. The average dissolution rate for carbonate minerals is more than 10 orders of magnitude greater than the dissolution rate of clays [e.g., *Köhler et al.*, 2003], so that these minerals can be considered as kinetically inactive compared to carbonate minerals, although their reactive surface is much larger. Thus the clay dissolution is considered to be negligible in the experiment. Only cation exchange should be considered.

[57] The Ca and Mg concentrations were variable during the experiment. Because the fluid resident time is about three time higher for stages 2 to 5 at 100 cm^3 h^{-1} than for stage 1 at 300 cm^3 h^{-1}, the chemical reactions progress further toward equilibrium during stages 2 to 5 than stage 1. This explains the discontinuity in the evolution of Ca and Mg concentration between stage 1 and stage 2 (6.6 $\times$ 10^{-5} M at the end of stage 1 versus 1.2 $\times$ 10^{-4} M at the beginning of stage 2). However, examination of Figure 9 presenting the sample-scale flux (mol s^{-1}) of Ca and Mg, $F_{Ca} = Q\,C_{Ca}$ and $F_{Mg} = Q\,C_{Mg}$ shows that the dissolution of calcite and dolomite is enhanced by transport processes when the flow velocity increases. F_{Ca} is equal to 5.5 $\times$ 10^{-9} mol s^{-1} at the end of the flow-through stage 1 at 300 cm^3 h^{-1} and only to 3.2 $\times$ 10^{-9} mol s^{-1} at the beginning of the stage 2 at 100 cm^3 h^{-1}.

[58] As calcite comprises 89% and dolomite 11% of the carbonate phase, the ratio of n_{Ca}/n_{Mg} in the rock sample is theoretically equal to 17.2. Moreover, the calcite dissolution rate (r_{cal}) is expected to be 6 to 3 times greater than that of dolomite (r_{dol}) between pH 3.9 and 4.6, according to equations (10) and (11) [*Morse and Arvidson*, 2002]. It is expected that the ratio of F_{Ca}/F_{Mg} would be between $\sim$100 and 50 if the reactive surfaces of these two minerals were equal. In fact, the ratio of F_{Ca}/F_{Mg} remained approximately constant during the experiment, and the F_{Ca} is only about 11.3 $\pm$ 1.2 times higher than F_{Mg}. This result suggests that either the reactive surface of dolomite in this sample is about ten times greater than that of calcite or that the rate laws (equations (10)–(11)) are not appropriate for dolomite in this sample, which appears to be undergoing dedolomitization (see section 3.3.2).

4.4. Specific Surface Area Versus Reactive Surface Area

[59] The increase in roughness observed during the first stage of the experiment (section 4.1) can be related to an increase in the geometric surface area of the fracture walls. The specific surface S_s increases from 1.8 to 2.6 during the first stage of the experiment. In contrast, the value of F_{Ca} progressively decreased during the experiment, from 7.6 $\times$ 10^{-9} to 5.5 $\times$ 10^{-9} mol s^{-1} during stage 1 (corresponding to a decrease of 28% after 4 hours 30 min) and from 3.2 $\times$ 10^{-9} to 1.6 $\times$ 10^{-9} mol s^{-1} during stages 2 to 5 (corresponding

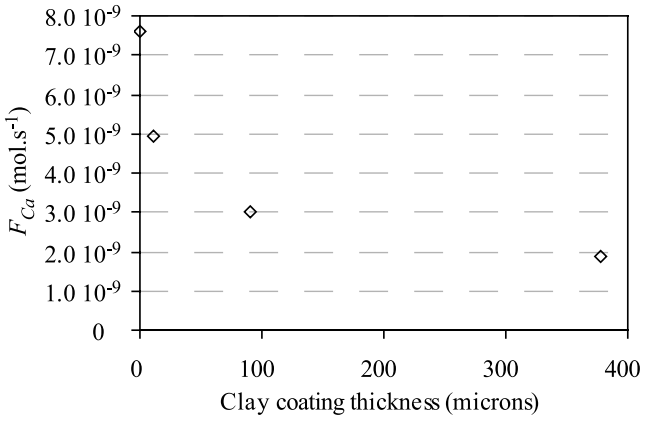

Figure 10. Measured chemical flux of Ca as a function of the clay coating thickness for the different flow-through stages.

to a decrease of 50% after 95 hours). The factors that contribute to the variation in the rate of calcite dissolution under acidic condition are changes in calcite reactive surface and mass transfer effects [e.g., *Lasaga*, 1998; *Lasaga and Kirkpatrick*, 1981]. The plane of the fracture is oriented approximately 80 degrees to the bedding plane. Therefore we can assume that the surface area of calcite $S_{S\text{-}Ca}$ exposed to the fluid does not vary significantly with time. However, this is not the case for the surface area of clays $S_{S\text{-}Cl}$ and quartz $S_{S\text{-}Qtz}$, which increases because of the disappearance of calcite. The development of the microporous phase essentially composed of clays increases the amount of reactive surface for sorption, which can have an impact on retardation of potential contaminants.

[60] The decrease of F_{Ca} results from increasing diffusion resistance to mass transfer of Ca from dissolving calcite surfaces to fluid moving through the fracture. Increased calcite dissolution increases the thickness of the layer of clay minerals and, therefore further increases the diffusion resistance to calcite dissolution. This observation clearly reveals the major role of the physical mass transfer rate limitations compared to chemical reaction rate limitations to controlling the sample-scale dissolution rate during the early stage of calcite/water interaction in the fracture.

4.5. Impact of the Alteration Film Development on Transport Processes

[61] The protective role of the clay coating is investigated by examining the variation of the rate of calcite dissolution versus the microporous clay coating thickness increase. The coating thickness (e_{film}) is calculated from the difference between the size of the aperture owing to calcite dissolution a_c and the actual size of the mechanical aperture a_m, and the measured volume percent of calcite in the rock (65%)

$$e_{film} = \frac{100}{65} a_c - a_m \tag{12}$$

[62] The decrease of F_{Ca} as a function of e_{film} is presented in Figure 10. The role of an alteration film to reduce the dissolution rate has been already observed by authors who have investigated the chemical alteration of limestone [*Roques and Ek*, 1973] or volcanic glass [*Techer et al.*, 2001], but no quantification of the relationship between the thickness of the alteration film and the kinetics of reaction have been reported.

[63] Reactive transport in a fracture involves chemical reactions in the matrix and the transport of the chemical elements both in the fracture void and in the matrix. However, solute transport within the low-permeable matrix can occur only by molecular diffusion. In contrast, flow in the highly permeable fracture involves advection and diffusion-dispersion phenomena. Moreover, the possible important feedback between changes in porosity induced by mineral reaction and changes in fluid flow must be taken into account.

[64] Figure 11 illustrates a conceptual model for the transport phenomena in the fracture at the beginning and throughout the experiment. At the start of the experiment, solute transport is advective and dispersive dominant in the flow direction. If we approximate the fracture morphology by a parallel plate model, transport is reduced to a 2-D diffusion-advection equation in the flow direction, as solved by *Berkowitz and Zhou* [1996]. The low-diffusion coefficient in the matrix makes it possible to introduce a constant

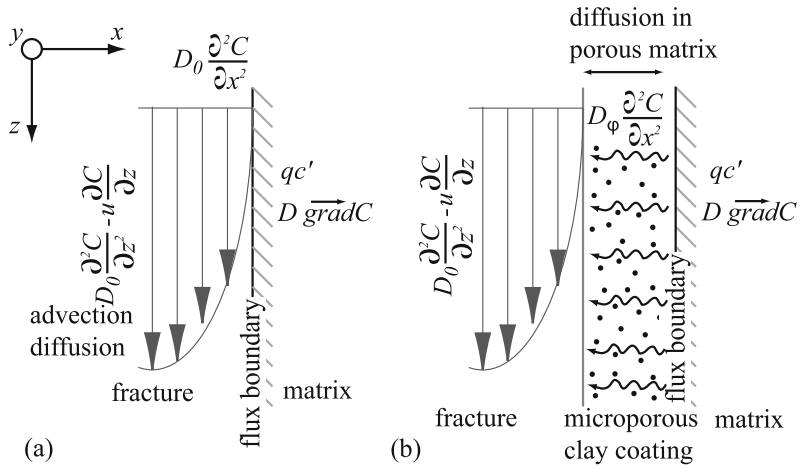

Figure 11. Schematic representation of the transport phenomena in the fracture (a) at the beginning of the experiment and (b) since the clay coating starts to form.

diffusive flux boundary condition at the fracture surface [*Steefel and Lichtner*, 1998], assuming that diffusive fluxes within the matrix can be neglected because they are small compared to those in the fracture void.

[65] As the clay coating develops, the porosity increase in the rock matrix affects the coupled reaction and transport processes. The access of reactants to the calcite surface and the departure of the reaction products from the surface are impeded by the development of the microporous clay coating. The clay coating so formed acts as a diffusive barrier to the chemical reactants and products that contributes to the control of the global reaction kinetics. As the fluid velocity in the microporous clay coating is negligible compared to that in the fracture void, solute transport within the alteration film can be reduced to transverse molecular diffusion. However, assuming a constant-diffusion coefficient in the matrix is unreasonable. For example, *Sakagius and Neretnieks* [1986] and *Bradbury and Green* [1986] observed that an altered zone can increase matrix diffusion compared to the same nonaltered massive rock, whose diffusivity can increase by a factor ranging from 20 to 200. The effective diffusion coefficient, $D_{e(\phi)}$, increases with dissolution of the carbonate grains, increasing porosity and decreasing tortuosity in the altered clay coating. Thus the value of $D_{e(\phi)}$ varies in time and space and feedback must be introduced between mineral reaction and D_e. It can be expressed using Archie's law [*Archie*, 1942].

[66] Finally, the assumption of a constant diffusive flux boundary at the fracture wall surface is unsuitable. The constant flux boundary condition moves as dissolution of carbonate grains occurs in the matrix. Accounting for matrix diffusion and interface displacement complicates quantification of solute transport in the fracture.

4.6. Application to the Development of Preferential Flow Paths in Fractured Rocks

[67] The present study illustrates the potential of carbonate-associated minerals to substantially modify the transport mechanism within a fracture. In a pure limestone fracture, transport is expected to be advective and dispersive dominant in the flow direction. Two characteristics are expected to control the transport and the rate of fracture opening with time: the chemical reaction rate and the flow velocity field. The two dimensionless parameters that can account for the relative contributions of advection, diffusion and chemical reaction in the mass transfer process are the Damköhler number ($Da = k_d L^*/u$) and the Peclet number ($Pe = uL^*/D_m$), where u is the fluid velocity [$L\ T^{-1}$], k_d is a first-order rate constant [T^{-1}], L^* is a characteristics length [L], and D_m is the molecular diffusion coefficient [$L^2\ T^{-1}$]. *Da* compares the relative influence of chemical reaction rates on advective transport. *Pe* compares the relative magnitude of advective to diffusive transport. When *Da* is large, the rate of the chemical reaction is larger than the rate at which the fluid is transported. In this case, dissolution patterns depend largely on the Peclet number, as observed by *Detwiler et al.* [2003]. At high *Pe* (advective-dominated transport), the dissolution is relatively homogeneous whereas at low *Pe* (diffusive-dominated transport) flow localizes in preferential channels. The process that accelerates flow localization and channel growth is the reactive infiltration instability described by *Ortoleva et al.* [1987a]. Initial heterogeneities in the fracture aperture cause the flow to be localized in preferential paths. Since the permeability is larger within preferential paths, flow and transport is focused within these paths leading to a rapid enlargement of the channels and slower dissolution outside the channels. Thus it is expected that the development of channels is related to initial heterogeneities of the fracture aperture and flow field.

[68] However, *Noiriel et al.* [2007], who investigated dissolution effects in a slightly argillaceous limestone, demonstrated that transport in the presence of silicate minerals in the rock appears more unpredictable than experimentally observed or numerically modeled in monomineralic rocks. In the present study, the clay and other silicate minerals remained in the fracture void after carbonate minerals had dissolved. Although heterogeneities are initially present and flow along the fracture is expected to generate preferential dissolution near the fracture inlet, where chemical disequilibrium and therefore rate for calcite dissolution is higher, the thickness of the clay coating is relatively homogeneous. Despite high values of *Da* and *Pe* in the experiment, channel growth was not observed. This observation suggests that the coating tends to dissipate the chemical gradients near the fracture surface. Consequently, the presence of silicate minerals impeded calcite dissolution process by impeding the transport of reactants and products to and from the calcite surface. Moreover, increasing the coating thickness can dramatically reduce the permeability within the fracture and reorganize the flow paths. Taken together, these observations suggest that dissolution in a fracture when coupled with development of a coating favors neither a rapid enlargement of the fracture aperture nor the development of preferential flow paths.

5. Conclusion

[69] The relation between decreasing dissolution rate of calcite and increasing duration of chemical alteration was investigated in an acidic water percolation experiment. The results of this experiment identify the controls exerted by mineral dissolution on flow and transport inside a fracture in an argillaceous limestone. The observed mineralogical heterogeneities of the rock matrix, in combination with differences between dissolution rates of the various minerals present in the rock and the reorganization of the clay and other silicate minerals have a strong influence on dissolution processes and hydraulic properties in the fracture. Calcite dissolution, reorganization (and, in places, displacement) of clay minerals in the fracture occur concurrently. The decrease in the rate of carbonate dissolution results from the development at the fracture surface of a microporous clay coating. This film forms a diffusive barrier to the reactants and products that migrate to and from the calcite surface. The growth of the clay coating coupled with the dissolution of carbonates progressively leads to clay reorganization. Despite the dissolution of calcite, the permeability does not increase as might be expected. Moreover, the growth of this coating progressively weakens its mechanical cohesion and clays are removed when the cohesive strength becomes lower than the strength exerted by the flowing fluid. Then, the massive displacement of clays leads to the clogging of the fracture. The results presented in this paper suggest that the development of a clay coating at the fracture surface may significantly alter the transport prop-

erties within the fracture, thereby affecting the permeability and the location of preferential flow pathways. These experimental findings demonstrate that reorganization of clay minerals can lead to a reduction in fracture permeability even under chemical conditions that favor carbonate dissolution. This work demonstrates the capability of using high-resolution 3-D images from X-ray microtomography experiments to follow and characterize dynamic Earth alteration processes.

[70] **Acknowledgments.** This project was partially supported by the French ministry of Research (MENRT grant to C. Noiriel). We wish to thank sincerely Douglas B. Kent (Associate Editor), the reviewers, and Françoise Poirier for their constructive comments, suggestions, and contributions. We also acknowledge support from the European Synchrotron Radiation Facility under project ME-572. We thank Xavier Thibault, Elodie Boller and Peter Cloetens (ESRF-ID19) for their helpful assistance in the XCMT scanning. We also appreciate the contribution of Daniel Garcia (École des Mines de Saint-Etienne) for chemical analysis and Benoit Vincent (Institut Français du Pétrole) for the petrographic interpretation.

References

Anbeek, C. (1992), Surface roughness of minerals and implications for dissolution studies, *Geochem. Cosmochim. Acta*, *56*, 1461–1469.

Archie, G. E. (1942), The electrical resistivity log as an aid to determining some reservoir characteristics, *Trans. Am. Inst. Min. Eng.*, *146*, 54–61.

Bassett, W., and T. Wu (1999), Real-time X-ray diffraction of montmorillonite dehydration and rehydration at pressure and temperature in a diamond anvil cell, in *Synchrotron X-Ray Methods in Clay Science*, edited by D. G. Schulze, J. W. Stucki, and P. M. Bertsch, pp. 220–240, Clay Miner. Soc., Chantilly, Va.

Békri, S., J. F. Thovert, and P. M. Adler (1997), Dissolution and deposition in fractures, *Eng. Geol.*, *48*, 283–308.

Berkowitz, B., and J. Zhou (1996), Reactive solute transport in a single fracture, *Water Resour. Res.*, *32*, 901–913.

Bradbury, M. H., and A. Green (1986), Investigations into the factors influencing long range matrix diffusion rates and pore space accessibility at depth in granite, *J. Hydrol.*, *89*, 123–139.

Brown, S. R. (1987), Fluid flow through rock joints: The effect of surface roughness, *J. Geophys. Res.*, *92*, 1337–1347.

Brunauer, S., P. H. Emmet, and E. A. Teller (1938), Adsorption of gases in multimolecular layers, *J. Am. Chem. Soc.*, *60*, 309–319.

Brush, D. J., and N. R. Thomson (2003), Fluid flow in synthetic rough-walled fractures: Navier-Stokes, Stokes, and local cubic law simulations, *Water Resour. Res.*, *39*(4), 1085, doi:10.1029/2002WR001346.

Carman, P. C. (1937), Fluid flow through granular beds, *Trans. Inst. Chem. Eng.*, *15*, 150–166.

Cheung, W., and H. Rajaram (2002), Dissolution finger growth in variable aperture fractures: Role of the tip-region flow field, *Geophys. Res. Lett.*, *29*(22), 2075, doi:10.1029/2002GL015196.

Chou, L., R. M. Garrels, and R. Wollast (1989), Comparative study of the kinetics and mechanisms of dissolution of carbonate minerals, *Chem. Geol.*, *78*, 269–282.

Crovisier, J. L., T. Advocat, and J. L. Dussossoy (2003), Nature and role of natural alteration gels formed on the surface of ancient volcanic glasses (natural analogs of waste containment glasses), *J. Nucl. Mater.*, *321*, 91–109.

Cubillas, P., S. Kohler, M. Prieto, C. Chairat, and E. H. Oelkers (2005), Experimental determination of the dissolution rates of calcite, aragonite, and bivalves, *Chem. Geol.*, *216*, 59–77.

Detwiler, R. L., R. J. Glass, and W. L. Bourcier (2003), Experimental observations of fracture dissolution: The role of Peclet number on evolving aperture variability, *Geophys. Res. Lett.*, *30*(12), 1648, doi:10.1029/2003GL017396.

Dijk, P., B. Berkowitz, and P. Bendel (1999), Investigation of flow in water-saturated rock fractures using nuclear magnetic resonance imaging (NMRI), *Water Resour. Res.*, *35*, 347–360.

Dijk, P. E., B. Berkowitz, and Y. Yechieli (2002), Measurement and analysis of dissolution patterns in rock fractures, *Water Resour. Res.*, *38*(2), 1013, doi:10.1029/2001WR000246.

Durham, W. B., W. L. Bourcier, and E. A. Burton (2001), Direct observation of reactive flow in a single fracture, *Water Resour. Res.*, *37*, 1–12.

Gautier, J. M., E. H. Oelkers, and J. Schott (2001), Are quartz dissolution rates proportional to BET surface areas?, *Geochem. Cosmochim. Acta*, *65*, 1059–1070.

Glover, P. W. J., K. Matsuki, R. Hikima, and K. Hayashi (1997), Fluid flow in fractally rough synthetic fractures, *Geophys. Res. Lett.*, *24*, 1803–1806.

Gonzales, R. C., and R. E. Woods (1992), *Digital Image Processing*, 716 pp., Addison-Wesley, Boston, Mass.

Gouze, P., C. Noiriel, C. Bruderer, D. Loggia, and R. Leprovost (2003), X-ray tomography characterization of fracture surfaces during dissolution, *Geophys. Res. Lett.*, *30*(5), 1267, doi:10.1029/2002GL016755.

Hakami, E., and E. Larsson (1996), Aperture measurements and flow experiments on a single natural fracture, *Int. J. Rock Mech. Min. Sci. Geomech. Abstr.*, *33*, 395–404.

Hanna, R. B., and H. Rajaram (1998), Influence of aperture variability on dissolutional growth of fissures in karst formations, *Water Resour. Res.*, *34*, 2843–2854.

Herman, G. T. (1980), *Image Reconstruction From Projections: Fundamentals of Computerized Tomography*, 316 pp., Academic, New York.

Köhler, S., F. Dufaud, and E. H. Oelkers (2003), An experimental study of illite dissolution rates as a function of pH from 1.4 to 12.4 and temperature from 5 to 50°C, *Geochem. Cosmochim. Acta*, *67*, 3583–3594.

Komine, H. (2004), Simplified evaluation on hydraulic conductivities of sand-bentonite mixture backfill, *Appl. Clay Sci.*, *26*, 13–19.

Lasaga, A. C. (1998), *Kinetic Theory in the Earth Sciences*, 811 pp., Princeton Univ. Press, Princeton, N. J.

Lasaga, A. C., and R. J. Kirkpatrick (Eds.) (1981), *Kinetics of Geochemical Processes*, *Rev. Mineral.*, vol. 8, 398 pp., Mineral. Soc. of Am., Washington, D. C.

Ledieu, A. (2004), Altération par l'eau des verres borosilicatés: Expériences, modélisation et simulations Monte Carlo, 176 pp., these, Ecole Polytech., Paris.

Mees, F., R. Swennen, M. Van Geet, and P. Jacobs (Eds.) (2003), *Applications of X-ray Computed Tomography in the Geosciences*, *Geol. Soc. Spec. Publ.*, *215*, 243 pp.

Méheust, Y., and J. Schmittbuhl (2000), Flow enhancement in a rough fracture, *Geophys. Res. Lett.*, *27*, 2989–2992.

Morse, J. W., and R. S. Arvidson (2002), The dissolution kinetics of major sedimentary carbonate minerals, *Earth Sci. Rev.*, *58*, 51–84.

Murphy, W. M., E. H. Oelkers, and P. C. Lichtner (1989), Surface reaction versus diffusion control of mineral dissolution and growth rates in geochemical processes, *Chem. Geol.*, *78*, 357–380.

Myers, N. O. (1962), Characterization of surface roughness, *Wear*, *5*, 182–189.

Noiriel, C., P. Gouze, and B. Madé (2007), Time-resolved 3D characterisation of flow and dissolution patterns in a single rough-walled fracture, in *IAH Selected Papers Series 9 on Groundwater in Fractured Rocks*, edited by J. Krasny and J. Sharp, Taylor and Francis, Philadelphia, Pa., in press.

Norrish, K. (1954), The swelling of montmorillonite, *Disc. Faraday Soc.*, *18*, 120–134.

Ortoleva, P., E. Merino, C. Moore, and J. Chadam (1987a), Geochemical self-organization I. Reaction - transport feedbacks and modeling approach, *Am. J. Sci.*, *287*, 979–1007.

Ortoleva, P. J., J. Chadam, E. Merino, and A. Sen (1987b), Geochemical self-organization II. The reactive infiltration instability, *Am. J. Sci.*, *287*, 1008–1040.

Pitas, I. (2000), *Digital Image Processing Algorithms and Applications*, 432 pp., John Wiley, Hoboken, N. J.

Plummer, L. N., T. M. L. Wigley, and D. L. Parkhurst (1978), The kinetics of calcite dissolution in CO_2-water systems at 5° to 60°C and 0.0 to 1.0 atm CO_2, *Am. J. Sci.*, *278*, 179–216.

Polak, A., D. Elsworth, J. Liu, and A. S. Grader (2004), Spontaneous switching of permeability changes in a limestone fracture with net dissolution, *Water Resour. Res.*, *40*, W03502, doi:10.1029/2003WR002717.

Prost, R. (1990), Organisation des matériaux argileux en relation avec leur comportement hydrique, in *Matériaux Argileux: Structure, Propriétés et Applications*, edited by A. Decarreau, pp. 387–440, Soc. Fr. de Minéral. et de Cristallogr.–Groupe Fr. des Argiles, Paris.

Rickard, D., and E. L. Sjöberg (1983), Mixed kinetic control of calcite dissolution rates, *Am. J. Sci.*, *283*, 815–830.

Roques, H., and C. Ek (1973), Etude expérimentale de la dissolution de calcaires par une eau chargée en CO_2, *Ann. Speleol.*, *28*, 549–563.

Sakagius, K., and I. Neretnieks (1986), Porosities and diffusivities of some nonsorbing species in crystalline rocks, *Water Resour. Res.*, *22*, 389–398.

Scheidegger, A. E. (1957), *The physics of flow through porous media*, 236 pp., Univ. of Toronto Press, Toronto, Ont., Canada.

Schmittbuhl, J., F. Schmitt, and C. Scholz (1995), Scaling invariance of crack surfaces, *J. Geophys. Res.*, *100*, 5953–5973.

Serra, H., P. Dudoignon, and C. Guy (1998), The role of smectite in the clogging mechanism of microcracks: Example of water/hawaiite interaction, *C. R. Acad. Sci.*, *226*, 93–99.

Sjöberg, E. L., and D. Rickard (1984), Temperature dependence of calcite dissolution kinetics between 1 and 62°C at pH 2.7 to 8.4 in aqueous solutions, *Geochem. Cosmochim. Acta*, *48*, 485–493.

Steefel, C. I., and A. C. Lasaga (1990), Evolution of dissolution patterns: Permeability change due to coupled flow and reaction, in *Chemical Modeling of Aqueous Systems II*, pp. 212–225, Am. Chem. Soc., Washington, D. C.

Steefel, C. I., and P. C. Lichtner (1998), Multicomponent reactive transport in discrete fractures: I. Controls on reaction front geometry, *J. Hydrol.*, *209*, 186–199.

Techer, I., T. Advocat, J. Lancelot, and J. M. Liotard (2001), Dissolution kinetics of basaltic glasses: Control by solution chemistry and protective effect of the alteration film, *Chem. Geol.*, *176*, 235–263.

Thompson, M. E., and S. R. Brown (1991), The effect of anisotropic surface roughness on flow and transport in fractures, *J. Geophys. Res.*, *96*, 21,923–21,932.

van der Lee, J. (1998), Thermodynamic and mathematical concepts of CHESS, *Tech. Rep. LHM/RD/98/3*, 99 pp., Ecole des Mines de Paris, Fontainebleau, France.

Weisbrod, N., R. Nativ, E. M. Adar, D. Ronen, and A. Ben-Nun (2000), Impact of coating and weathering on the properties of chalk fracture surfaces, *J. Geophys. Res.*, *105*, 27,853–27,864.

Wersin, P., E. Curti, and C. A. J. Appelo (2004), Modelling bentonite-water interactions at high solid/liquid ratios: Swelling and diffuse double layer effects, *Appl. Clay Sci.*, *26*, 249–257.

White, A. F., and S. L. Brantley (1995), *Chemical Weathering Rates of Silicate Minerals: An Overview*, *Rev. Mineral.*, vol. 31, 583 pp., Mineral. Soc. of Am., Washington, D. C.

White, A. F., and S. L. Brantley (2003), The effect of time on the weathering of silicate minerals: Why do weathering rates differ in the laboratory and field?, *Chem. Geol.*, *202*, 479–506.

White, A. F., T. D. Bullen, D. V. Vivit, M. S. Schulz, and D. W. Clow (1999), The role of disseminated calcite in the chemical weathering of granitoid rocks, *Geochem. Cosmochim. Acta*, *63*, 1939–1953.

Zimmerman, R. W., and G. S. Bodvarsson (1996), Hydraulic conductivity of rock fractures, *Transp. Porous Media*, *23*, 1–30.

Zimmerman, R. W., and I. Yeo (2000), Fluid flow in rock fractures: From the Navier-Stokes equations to the cubic law, in *Dynamics of Fluids in Fractured Rocks*, *Geophys. Monogr. Ser.*, vol. 122, edited by B. Faybishenko, P. A. Witherspoon, and S. M. Benson, pp. 213–224, AGU, Washington, D. C.

Zimmerman, R. W., D. Chen, and G. W. Cook (1992), The effect of contact area on the permeability of fractures, *J. Hydrol.*, *139*, 79–96.

P. Gouze, Laboratoire Géosciences, Université de Montpellier II, CNRS, F-34095 Montpellier, France.

B. Madé, Centre de Géosciences, École des Mines de Paris, UMPC, EPHE, CNRS, F-77305 Fontainebleau, France.

C. Noiriel, Laboratoire Processus et Bilans des Domaines Sédimentaires, Université de Lille I, Bat. SN5, F-59650 Villeneuve d'Ascq cedex, France. (catherine.noiriel@univ-lille1.fr)